Progress In Electromagnetics Research C, Vol. 128, 207–218, 2023

Anisotropy Analysis of the 3D-Radial Point Interpolation Method in Lossy Media

Naamen Hichem[1, *], Ajmi B. H. Hamouda[2], and Taoufik Aguili[1]

Abstract—This paper presents the general numerical dispersion relationship for the three-dimensional (3-D) Radial Point Interpolation (RPIM) method in lossy media. A similar analysis has also been carried out and compared with the traditional Finite-Difference Time-Domain (FDTD) method. Both methods investigate dispersion, numerical loss, and anisotropy versus electric conductivity. The RPIM reveals lower numerical loss errors (NLE) over a wide conductivity range at the considered frequency. Furthermore, the numerical experiments show that a slight increase in the conductivity, for the lossless case, has almost removed the numerical anisotropy dispersion, which improves the numerical resonance frequency precision. Therefore, this effect can be used as an anisotropy optimization technique for lossless media. Based on a close examination of the experimental results around the resonant frequency, the numerical error for the lossless case was divided by ten. As a result, the experimental and theoretical resonance frequencies are found to be in good agreement.

1. INTRODUCTION

A variety of typical engineering applications look to numerical simulation techniques for solving practical and complex problems [1, 2], as well as for solving Maxwell's equations in the time domain for electromagnetic modelling purposes. Among these methods, RPIM is technically a meshless method [2], where spread nodes within a domain are either structurally unconnected, uniformly, or randomly distributed, but are connected inherently through shape functions that convey the detailed geometry. Hence, multiscale node distributions based on selective finite discretization are used for modelling complex geometries in fairly precise detail [3]. Additionally, adaptive refinement is an advantage that arises from the simplicity in the distribution of nodes, which may enhance simulation accuracy [4, 5]. It should also be noted that the derivatives of the E/H shape functions, calculated by interpolation, provide a numerical alternative to estimate the spatial curls [6] in steady-state Maxwell's equations.

The finite-difference scheme involved in classical numerical mesh methods generates, in a deterministic approach, numerical dispersion induced by the phase velocity variation as a function of frequency, numerical anisotropy characterized by the phase velocity varying with the propagation direction, and numerical dissipation causing amplitude errors [7]. Thus, the numerical anisotropy is a spectral concept which results in the spatio-temporal domain by a distortion of the wave [20, 21]. By transcending the finite-difference scheme, numerical dispersion of RPIM comes directly from interpolating the unknown fields over the shape functions under study.

A study of RPIM numerical dispersion has been carried out in [8] by applying the spectral Fourier transform to the time-stepping equations for the leapfrog scheme. To reveal its specific characteristics, the dispersion analysis of RPIM in a 3D problem involving a lossy media is needed, since the wavenumber is complex [9]. However, this differs from the assumption of lossless media that involves purely

Received 29 September 2022, Accepted 28 December 2022, Scheduled 12 January 2023

* Corresponding author: Naamen Hichem (naamen.hichem123@gmail.com).

[1] Technology Department of Information and Communications, National Engineering School at Tunis, Tunisia. [2] Quantum and Statistical Physics Laboratory, Faculty of Sciences, University of Monastir, Tunisia.

real wavenumbers. The transition matrix ensures the temporal evolution of the fields in the whole domain. The basic procedure for the numerical dispersion analysis involves the substitution of a plane, monochromatic, travelling electromagnetic wave into these leapfrog meshless RPIM formulations. Thus, the numerical dispersion relation is derived that relates the numerical wave vector components, wave frequency, time-step, and spatial resolution. Such a procedure is pursued for the RPIM and FDTD. The dispersion relation is numerically solved using Newton's method [10].

Therefore, by analysing numerical RPIM dispersion and dissipation characteristics, the numerical phase error NPE, numerical loss error NLE, numerical anisotropy loss A_l, and dispersion A_d are calculated as functions of the media conductivity in different directions. Having numerically derived their respective dispersion relations, the results are compared with those obtained using the FDTD procedure. Our numerical results indicate that the RPIM has higher accuracy in a wide conductivity range, despite a trade-off between their inner dispersion characteristics. For both methods at the considered frequency, the numerical anisotropy dispersion reaches zero when the electric conductivity equals 0.0288 S/m. This behaviour is exploited in the RPIM in order to minimize numerical anisotropy dispersion in lossless media.

2. RADIAL POINT INTERPOLATION METHOD (RPIM) ALGORITHM

Let $u(X)$ be a scalar function defined in the problem domain. By forcing the interpolation function to pass through the function values at every node within the defined support domain, the RPIM interpolates $u(X)$ around every node $X(x, y, z)$. Using polynomial basis functions in the RPIM, the field variable functions are interpolated as follows:

$$u(X) = \sum_{i=1}^{i=N} R_i(X)a_i + \sum_{j=1}^{j=M} P_j(X)b_j, \tag{1}$$

where $R_i(X)$ and $P_j(X)$ are radial and polynomial basis functions, respectively. a_i and b_j are the associated interpolation coefficients to be determined. N and M are the numbers of basis functions and polynomial basis terms, respectively, in the support domain. The Gaussian function is selected to be radial, with shape parameter α to adjust the decaying degree. Thus, the radial basis function (RBF) is given by:

$$r_n(X) = \exp\left[-\alpha\left(r/r_{\max}\right)^2\right], \tag{2}$$

where $r = \sqrt{(x-x_n)^2 + (y-y_n)^2 + (z-z_n)^2}$ is the distance between the point of interest X and a node at $X_n(x_n, y_n, z_n)$, and $r_{\max}$ is the maximum distance between the selected point to be interpolated and the nodes in the support domain. Usually the number N of radial basis terms is greater than M. Thus, linear monomial basis functions with four terms ($M = 4$) are adopted to build the polynomial basis $[1, x, y, z]$. Therefore, at the point X, Equation (1) can be written:

$$u(X) = \mathbf{R}^{\mathsf{T}}(X)\mathbf{a} + \mathbf{P}^{\mathsf{T}}(X)\mathbf{b}, \tag{3}$$

where $\mathbf{a}$ and $\mathbf{b}$ are coefficient vectors. T denotes the matrix transpose symbol; $\mathbf{R}^{\mathsf{T}}(X)$ and $\mathbf{P}^{\mathsf{T}}(X)$ are radial and polynomial basis vectors, respectively, given by:

$$\mathbf{R}^{\mathsf{T}}(X) = [r_1(X), r_2(X), \ldots, r_N(X)], \tag{4}$$

$$\mathbf{P}^{\mathsf{T}}(X) = [p_1(X), p_2(X), p_3(X), p_4(X)] = [1, x, y, z]. \tag{5}$$

A linear system is built by forcing $u(X)$ to pass through every scattered node in the field's support domain at the point of interest X. This formulation relates the accurate values of field variables at the N nodes in the support domain to the unknown interpolation coefficients. The linear algebraic system expressed as a matrix equation is given by:

$$\mathbf{U}_s = \mathbf{R}_0 \cdot \mathbf{a} + \mathbf{P}_0 \cdot \mathbf{b}, \tag{6}$$

where $\mathbf{U}_s$ is the vector that collects the field component values at the N nodes; $\mathbf{R}_0$ and $\mathbf{P}_0$ are moments matrices combining the radial basis $\mathbf{R}(X)$ and polynomial ones $\mathbf{P}(X)$, respectively, and evaluated at the N nodes within the support domain. The polynomial terms of the basis functions must support an

additional condition to ensure a unique solution for the set of homogeneous equations [5]. Therefore, the following condition should be satisfied:

$$\mathbf{P}_0^{\mathsf{T}} \cdot \mathbf{a} = \mathbf{0}. \tag{7}$$

Equations (6) and (7) can be recast into matrix form:

$$\mathbf{G}\begin{pmatrix}\mathbf{a}\\ \mathbf{b}\end{pmatrix} = \begin{pmatrix}\mathbf{R}_0 & \mathbf{P}_0\\ \mathbf{P}_0^{\mathsf{T}} & \mathbf{0}\end{pmatrix}\begin{pmatrix}\mathbf{a}\\ \mathbf{b}\end{pmatrix} = \begin{pmatrix}\mathbf{U}_s\\ \mathbf{0}\end{pmatrix}. \tag{8}$$

The moment matrix $\mathbf{R}_0$ is $N \times N$, and the matrix $\mathbf{P}_0$ is an $N \times M$. Since $\mathbf{R}_0$ is symmetric, the system of block matrix $\mathbf{G}$ will be too. If $\mathbf{G}$ is invertible, the corresponding solution is unique for interpolation vectors $\mathbf{a}$ and $\mathbf{b}$. By exploiting the non-singular property of matrix $\mathbf{R}_0$, we obtain:

$$\mathbf{b} = \mathbf{S}_b\mathbf{U}_s, \quad \mathbf{S}_b = \left[\mathbf{P}_0^{\mathsf{T}}\mathbf{R}_0^{-1}\mathbf{P}_0\right]^{-1}\mathbf{P}_0^{\mathsf{T}}\mathbf{R}_0^{-1}, \tag{9}$$

$$\mathbf{a} = \mathbf{S}_a\mathbf{U}_s, \quad \mathbf{S}_a = \mathbf{R}_0^{-1} - \mathbf{R}_0^{-1}\mathbf{P}_0\mathbf{S}_b. \tag{10}$$

In summary, the interpolation Equation (1) is written, in a vector form as:

$$u(X) = \left[\mathbf{R}^{\mathsf{T}}(X)\mathbf{S}_a + \mathbf{P}^{\mathsf{T}}(X)\mathbf{S}_b\right]\mathbf{U}_s = \mathbf{\Phi}(X)\mathbf{U}_s. \tag{11}$$

The vector $\mathbf{\Phi}(X)$ is an N-tuple whose entries are the shape functions:

$$\mathbf{\Phi}(X) = \mathbf{R}^{\mathsf{T}}(X)\mathbf{S}_a + \mathbf{P}^{\mathsf{T}}(X)\mathbf{S}_b = \left[\phi_1(X), \phi_2(X), \ldots, \phi_N(X)\right], \tag{12}$$

and $\phi_k(X)$ is the kth-node shape function in the considered support domain, expressed as:

$$\phi_k(X) = \sum_{i=1}^{i=N} R_i(X)\mathbf{S}_{ik}^a + \sum_{j=1}^{j=M} P_j(X)\mathbf{S}_{jk}^b. \tag{13}$$

Here $\mathbf{S}_{ik}^a$ and $\mathbf{S}_{jk}^b$ are the (ik) and (jk) elements of constant matrices, respectively. Thus, the derivatives of shape functions can be deduced analytically. With $\xi = x, y$ or z, we find:

$$\frac{\partial\phi_k}{\partial\xi}(X) = \sum_{i=1}^{i=N}\frac{\partial R_i}{\partial\xi}(X)\mathbf{S}_{ik}^a + \sum_{j=1}^{j=M}\frac{\partial P_j}{\partial\xi}(X)\mathbf{S}_{jk}^b. \tag{14}$$

Since RBF has a Gaussian form, the first derivative in Equation (14) is readily calculated, giving:

$$\frac{\partial R_i}{\partial\xi}(X) = \frac{-2\alpha}{r_{\max}^2}\left(\xi - \xi_i\right)R_i\left(x, y, z\right). \tag{15}$$

3. RPIM MAXWELL'S EQUATIONS IN LOSSY MEDIA

To implement the meshless RPIM technique in three dimensions, one must define two complementary sets of electric field nodes (E-nodes) and magnetic field nodes (H-nodes). However, in contrast to the FDTD method, all three components of the electric field are placed at the same E-node. The same applies to the magnetic field. The coupling aspect of electric and magnetic field components requires that each E-node should be surrounded by H-nodes and vice-versa [19].

In this paper, E-and H-nodes are spread similarly to the point-matched time-domain finite-element method [11]. Hence, each (i, j, k) E-node is surrounded by eight H-nodes, four at each of the $(k - 1/2)$ and $(k + 1/2)$ planes. In summary, we have selected eight surrounding H-nodes in the support domain of E-node and vice versa [13]. The ideal distribution of nodes is obtained with a high number of nodes per support domain, but this will increase the computational cost through the corresponding shape functions. For 3D problems, the minimal number of nodes per support domain is eight [Fig. 11] and four for 2D problems. The grids used by the RPIM are not necessarily regular as for the FDTD since they match the edge of the curves and avoid the problem of discontinuity (at the staircase) encountered in the FDTD. Once the dual node distributions have been generated in the 3D domain, the E/H shape functions with their derivatives are approximated using Equations (13) and (14). Thus, eight H-node

fields belonging to the E-node support domain will update the E-node field and vice versa [13]. The topological node connectivity is handled by processed shape functions with minimal loss of geometrical information.

The electromagnetic fields are considered in a sourceless region, filled with linear, isotropic, non-dispersive, and lossy medium. In Cartesian coordinates, the time-dependent 3D Maxwell's curl equations in differential form are stated as:

$$\nabla \wedge \vec{H} = \overline{\overline{M}}_{\varepsilon} \frac{\partial \vec{E}}{\partial t} + \overline{\overline{M}}_{\sigma} \vec{E}, \tag{16}$$

$$\nabla \wedge \vec{E} = -\overline{\overline{M}}_{\mu} \frac{\partial \vec{H}}{\partial t} - \overline{\overline{M}}_{\sigma^*} \vec{H}. \tag{17}$$

Here $\overline{\overline{M}}_{\varepsilon} = \overline{\overline{\text{diag}}}\{\varepsilon_x, \varepsilon_y, \varepsilon_z\}$, $\overline{\overline{M}}_{\mu} = \overline{\overline{\text{diag}}}\{\mu_x, \mu_y, \mu_z\}$, $\overline{\overline{M}}_{\sigma} = \overline{\overline{\text{diag}}}\{\sigma_x, \sigma_y, \sigma_z\}$ and $\overline{\overline{M}}_{\sigma^*} = \overline{\overline{\text{diag}}}\{\sigma_x^*, \sigma_y^*, \sigma_z^*\}$ are diagonal matrices with positive real elements composed of permittivity ε, permeability μ, electric conductivity σ, and equivalent magnetic loss σ^*.

A second-order centered difference approximates $[\partial \vec{E}/\partial t]^{n+1/2}$ and $[\partial \vec{H}/\partial t]^{n}$ by $(\vec{E}^{n+1} - \vec{E}^{n})/\Delta t$ and $(\vec{H}^{n+1/2} - \vec{H}^{n-1/2})/\Delta t$, respectively; i.e., $\vec{E}^{n+1/2}$ and $\vec{H}^{n}$ are estimated with second-order accuracy using the averages of the electric field at time levels n and $n+1$, and the magnetic field at time levels $n-1/2$ and $n+1/2$, respectively [12]. After several rearrangements, $\vec{E}^{n+1}$ and $\vec{H}^{n+1/2}$ at the E/H-node of interest $X_i^{E/H}$ lead to the following equations:

$$\begin{aligned} \vec{E}^{n+1}(X_i^E) \;=\; & \big[2\overline{\overline{M}}_{\varepsilon} + \Delta t \overline{\overline{M}}_{\sigma}\big]^{-1} \big[2\overline{\overline{M}}_{\varepsilon} - \Delta t \overline{\overline{M}}_{\sigma}\big] \vec{E}^{n}(X_i^E) \\ & + 2\Delta t \big[2\overline{\overline{M}}_{\varepsilon} + \Delta t \overline{\overline{M}}_{\sigma}\big]^{-1} \{\nabla \wedge \vec{H}^{n+1/2}\}(X_i^E), \end{aligned} \tag{18}$$

$$\begin{aligned} \vec{H}^{n+1/2}(X_i^H) \;=\; & \big[2\overline{\overline{M}}_{\mu} + \Delta t \overline{\overline{M}}_{\sigma^*}\big]^{-1} \big[2\overline{\overline{M}}_{\mu} - \Delta t \overline{\overline{M}}_{\sigma^*}\big] \vec{H}^{n-1/2}(X_i^H) \\ & - 2\Delta t \big[2\overline{\overline{M}}_{\mu} + \Delta t \overline{\overline{M}}_{\sigma^*}\big]^{-1} \{\nabla \wedge \vec{E}^{n}\}(X_i^H). \end{aligned} \tag{19}$$

Equation (11) permits the interpolation of $\vec{H}^{n+1/2}$ and $\vec{E}^{n}$ components over the H/E-shape functions inside their associate local support domains, leading to:

$$\{\nabla \wedge \vec{E}^{n}\}(X_i^H) \;=\; \sum_{j=1}^{j=N} \{\nabla \wedge \phi_j^E\}(X_i^H) \vec{E}_j^n = \overline{\overline{C}}_E \vec{E}^n, \tag{20}$$

$$\{\nabla \wedge \vec{H}^{n+1/2}\}(X_i^E) \;=\; \sum_{j=1}^{j=N} \{\nabla \wedge \phi_j^H\}(X_i^E) \vec{H}_j^{n+1/2} = \overline{\overline{C}}_H \vec{H}^{n+1/2},$$

with

$$\overline{\overline{C}}_E = \begin{pmatrix} \overline{\overline{0}}^E & -\overline{\overline{\phi}}_z^E & \overline{\overline{\phi}}_y^E \\ \overline{\overline{\phi}}_z^E & \overline{\overline{0}}^E & -\overline{\overline{\phi}}_x^E \\ -\overline{\overline{\phi}}_y^E & \overline{\overline{\phi}}_x^E & \overline{\overline{0}}^E \end{pmatrix}, \qquad \overline{\overline{C}}_H = \begin{pmatrix} \overline{\overline{0}}^H & -\overline{\overline{\phi}}_z^H & \overline{\overline{\phi}}_y^H \\ \overline{\overline{\phi}}_z^H & \overline{\overline{0}}^H & -\overline{\overline{\phi}}_x^H \\ -\overline{\overline{\phi}}_y^H & \overline{\overline{\phi}}_x^H & \overline{\overline{0}}^H \end{pmatrix}. \tag{21}$$

The superscript n is a temporal index; $\overline{\overline{0}}^{E/H}$ is the null matrix of appropriate dimensions; $\overline{\overline{C}}_E$ and $\overline{\overline{C}}_H$ are block matrices computed during the RPIM algorithm implementation and thoroughly described in [13]. The elements $\overline{\overline{\phi}}_{\xi}^{E/H}$ of $\overline{\overline{C}}_E/\overline{\overline{C}}_H$ are matrices collecting spatial E/H shape function derivatives for $\xi = x, y$, or z, for spread E/H nodes, evaluated at different $X_i^{H/E}$ nodes, respectively, and defined as:

$$\big[\phi_{\xi}^{E/H}\big]_{i,j} = \partial_{\xi} \phi_j^{E/H}(X_i^{H/E}). \tag{22}$$

After some algebraic manipulations, we cast Equations (18) and (19) into more compact vector-matrix form as:

$$\vec{E}^{n+1} \;=\; \overline{\overline{A}}_1 \vec{E}^{n} + \overline{\overline{A}}_2 \, \overline{\overline{C}}_H \cdot \vec{H}^{n+1/2}, \tag{23}$$

$$\vec{H}^{n+1/2} \;=\; \overline{\overline{B}}_1 \vec{H}^{n-1/2} - \overline{\overline{B}}_2 \, \overline{\overline{C}}_E \cdot \vec{E}^{n}. \tag{24}$$

$\overline{\overline{A}}_1$, $\overline{\overline{A}}_2$, $\overline{\overline{B}}_1$, and $\overline{\overline{B}}_2$ are constant diagonal matrices, expressed as:

$$\overline{\overline{A}}_1 = \left[2\overline{\overline{M}}_\varepsilon + \Delta t\overline{\overline{M}}_\sigma\right]^{-1}\left[2\overline{\overline{M}}_\varepsilon - \Delta t\overline{\overline{M}}_\sigma\right], \tag{25a}$$

$$\overline{\overline{B}}_1 = \left[2\overline{\overline{M}}_\mu + \Delta t\overline{\overline{M}}_{\sigma^*}\right]^{-1}\left[2\overline{\overline{M}}_\mu - \Delta t\overline{\overline{M}}_{\sigma^*}\right], \tag{25b}$$

$$\overline{\overline{A}}_2 = 2\Delta t\left[2\overline{\overline{M}}_\varepsilon + \Delta t\overline{\overline{M}}_\sigma\right]^{-1}, \tag{25c}$$

$$\overline{\overline{B}}_2 = 2\Delta t\left[2\overline{\overline{M}}_\mu + \Delta t\overline{\overline{M}}_{\sigma^*}\right]^{-1}. \tag{25d}$$

Substituting Equation (24) into (23) yields:

$$\vec{E}^{n+1} = \left[\overline{\overline{A}}_1 - \overline{\overline{A}}_2\overline{\overline{B}}_2\overline{\overline{C}}_H\overline{\overline{C}}_E\right]\vec{E}^n + \overline{\overline{A}}_2\overline{\overline{B}}_1\overline{\overline{C}}_H\vec{H}^{n-1/2}, \tag{26}$$

$$\vec{H}^{n+1/2} = -\overline{\overline{B}}_2\,\overline{\overline{C}}_E\cdot\vec{E}^n + \overline{\overline{B}}_1\vec{H}^{n-1/2}, \tag{27}$$

$$\vec{\psi}^{n+1} = \overline{\overline{G}}\cdot\vec{\psi}^n, \tag{28}$$

Equations (26) and (27) are combined into Equation (28), in matrix form, where $\vec{\psi}^n = \left[\vec{E}^n, \vec{H}^{n-1/2}\right]^\intercal = \left[\vec{E}_x^n, \vec{E}_y^n, \vec{E}_z^n, \vec{H}_x^{n-1/2}, \vec{H}_y^{n-1/2}, \vec{H}_z^{n-1/2}\right]^\intercal$ and $\overline{\overline{G}}$ is the transition matrix defined by:

$$\underset{\sigma\neq 0,\sigma^*\neq 0}{\overline{\overline{G}}} = \begin{pmatrix} \overline{\overline{A}}_1 - \overline{\overline{A}}_2\overline{\overline{B}}_2\overline{\overline{C}}_H\overline{\overline{C}}_E & \overline{\overline{A}}_2\overline{\overline{B}}_1\overline{\overline{C}}_H \\ -\overline{\overline{B}}_2\overline{\overline{C}}_E & \overline{\overline{B}}_1 \end{pmatrix}. \tag{29}$$

When the media is assumed electrically lossy ($\overline{\overline{M}}_{\sigma^*} = \bar{\bar{0}}_3$), the estimated transition matrix is given by:

$$\underset{\sigma\neq 0,\sigma^*=0}{\overline{\overline{G}}} = \begin{pmatrix} \overline{\overline{A}}_1 - \Delta t\overline{\overline{A}}_2\overline{\overline{M}}_\mu^{-1}\overline{\overline{C}}_H\overline{\overline{C}}_E & \overline{\overline{A}}_2\overline{\overline{C}}_H \\ -\Delta t\overline{\overline{M}}_\mu^{-1}\overline{\overline{C}}_E & \bar{\bar{I}}_3 \end{pmatrix}, \tag{30}$$

where $\bar{\bar{I}}_n$ is the $n\times n$ identity matrix. For the lossless case ($\overline{\overline{M}}_\sigma = \overline{\overline{M}}_{\sigma^*} = \bar{\bar{0}}_3$), the transition matrix $\overline{\overline{G}}$ is formulated as:

$$\underset{\sigma=0,\sigma^*=0}{\overline{\overline{G}}} = \bar{\bar{I}}_6 + \Delta t\overline{\overline{M}}_{\varepsilon,\mu}^{-1}\overline{\overline{C}} - (\Delta t)^2\overline{\overline{A}}, \tag{31}$$

with the matrices $\overline{\overline{M}}_{\varepsilon,\mu}$, $\overline{\overline{C}}$ and $\overline{\overline{A}}$ given by:

$$\overline{\overline{M}}_{\varepsilon,\mu} = \overline{\overline{\text{diag}}}\left\{\overline{\overline{M}}_\varepsilon, \overline{\overline{M}}_\mu\right\}, \tag{32a}$$

$$\overline{\overline{A}} = \overline{\overline{\text{diag}}}\left\{\overline{\overline{M}}_\varepsilon^{-1}\overline{\overline{M}}_\mu^{-1}\overline{\overline{C}}_H\overline{\overline{C}}_E, \bar{\bar{0}}\right\}, \tag{32b}$$

$$\overline{\overline{C}} = \begin{pmatrix} \bar{\bar{0}} & \overline{\overline{C}}_H \\ -\overline{\overline{C}}_E & \bar{\bar{0}} \end{pmatrix}. \tag{32c}$$

Note that these previous RPIM steady-state equations are identical to those given by the FDTD method unless the matrices $\overline{\overline{C}}_E$ and $\overline{\overline{C}}_H$ denote the numerical curl operators for the electric and magnetic fields in the discrete domain [7].

4. DISPERSION ANALYSIS OF THE RPIM IN LOSSY MEDIA

An analysis of RPIM and FDTD dispersion relations in lossy media is presented in this section. In order to illustrate this point, it is assumed that the traveling plane wave propagating in a lossy, homogeneous, and anisotropic media is monochromatic, sinusoidal, and TEM [14, 21], so that the field components at the nth time step are given by:

$$\vec{\psi} = \vec{\psi}_0 e^{\,j(\omega n\Delta t - k_x n_x\Delta x - k_y n_y\Delta y - k_z n_z\Delta z)}, \tag{33}$$

n_x, n_y, n_z, $k_x = k\sin(\theta)\cos(\phi)$, $k_y = k\sin(\theta)\sin(\phi)$, and $k_z = k\cos(\theta)$ are the three spatial integer-number indices and the three wavenumbers along the x, y, and z directions, respectively. Here k is

the numerical wavenumber, and (ϕ, θ) are the azimuthal and polar angles in a spherical coordinate system, respectively. Δx, Δy, and Δz are the uniform distances between neighboring E/H-nodes in the corresponding directions; ω is the angular frequency; and $\vec{\psi}_0$ is a vector that collects the initial values of the components of the electromagnetic fields. Equation (23) is rewritten under the following form, whereas Equation (27) remains unchanged:

$$\vec{E}^{n+1} - \overline{\overline{A}}_2 \overline{\overline{C}}_H \cdot \vec{H}^{n+1/2} = \overline{\overline{A}}_1 \vec{E}^n, \tag{34}$$

$$\vec{H}^{n+1/2} = -\overline{\overline{B}}_2 \, \overline{\overline{C}}_E \cdot \vec{E}^n + \overline{\overline{B}}_1 \vec{H}^{n-1/2}. \tag{35}$$

After substituting the general Fourier mode in time and space for both of the dependent electromagnetic variables, made by inserting Equation (33) into Equations (34) and (35), calculations detailed in [13] are considered. The resulting equations are written in the matrix form as:

$$\overline{\overline{G}}_1 \cdot \vec{\hat{\psi}}^{n+1} = \overline{\overline{G}}_2 \cdot \vec{\hat{\psi}}^{n}, \tag{36}$$

where, $\vec{\hat{\psi}}^{n} = [\hat{E}_x^n \; \hat{E}_y^n \; \hat{E}_z^n \; \hat{H}_x^{n-1/2} \; \hat{H}_y^{n-1/2} \; \hat{H}_z^{n-1/2}]^{\mathsf{T}}$, $\hat{E}_q^n$ and $\hat{H}_q^n$ are the field components in the spectral domain, $\overline{\overline{G}}_1$ and $\overline{\overline{G}}_2$ are iteration matrices for RPIM in the spectral domain, too. They are defined explicitly by the henceforth adopted notations:

$$\overline{\overline{G}}_1 = \begin{pmatrix} \overline{\overline{I}}_3 & 2C_2\overline{\overline{B}} \\ \overline{\overline{0}}_3 & \overline{\overline{I}}_3 \end{pmatrix}, \quad \overline{\overline{G}}_2 = \begin{pmatrix} C_1\overline{\overline{I}}_3 & \overline{\overline{0}}_3 \\ 2C_2'\overline{\overline{B}} & C_1'\overline{\overline{I}}_3 \end{pmatrix}, \tag{37}$$

where

$$C_1 = \frac{2\varepsilon - \sigma\Delta t}{2\varepsilon + \sigma\Delta t}, \qquad C_2 = \frac{2\Delta t}{2\varepsilon + \sigma\Delta t}, \tag{38a}$$

$$C_1' = \frac{2\mu - \sigma^*\Delta t}{2\mu + \sigma^*\Delta t}, \quad C_2' = \frac{2\Delta t}{2\mu + \sigma^*\Delta t}, \tag{38b}$$

$$\overline{\overline{B}} = \begin{pmatrix} 0 & -Q_z & Q_y \\ Q_z & 0 & -Q_x \\ -Q_y & Q_x & 0 \end{pmatrix}, \tag{38c}$$

and

$$Q_\xi = S_\xi W_\xi, \quad S_\xi = \frac{j}{\Delta\xi}, \tag{39a}$$

$$W_x = \sin\left(\frac{k_x\Delta x}{2}\right)\cos\left(\frac{k_y\Delta y}{2}\right)\cos\left(\frac{k_z\Delta z}{2}\right), \tag{39b}$$

$$W_y = \cos\left(\frac{k_x\Delta x}{2}\right)\sin\left(\frac{k_y\Delta y}{2}\right)\cos\left(\frac{k_z\Delta z}{2}\right), \tag{39c}$$

$$W_z = \cos\left(\frac{k_x\Delta x}{2}\right)\cos\left(\frac{k_y\Delta y}{2}\right)\sin\left(\frac{k_z\Delta z}{2}\right). \tag{39d}$$

Again $\xi = x, y, z$ are the propagation direction. Since the excitation is a monochromatic wave with a single angular frequency ω, we may write $\vec{\hat{\psi}}^{n} = \vec{\hat{\psi}}_0 \, e^{\,j\omega n\Delta t}$. Hence, Equation (36) can be written as:

$$\vec{\hat{\psi}}^{n+1} = \, e^{\,j\omega\Delta t}\vec{\hat{\psi}}^{n} = \, \overline{\overline{G}}_1^{-1} \cdot \overline{\overline{G}}_2 \, \vec{\hat{\psi}}^{n}. \tag{40}$$

For a homogeneous linear system, one can deduce:

$$\left(e^{\,j\omega\Delta t}\overline{\overline{I}}_6 - \overline{\overline{G}}_1^{-1} \cdot \overline{\overline{G}}_2\right) \cdot \vec{\hat{\psi}}^{n} = \overline{\overline{0}}_6. \tag{41}$$

By determining the determinant of the matrix in Equation (41) and setting it to zero, the resulting numerical dispersion relation for 3D-RPIM in lossy media can be written:

$$\sin^2\left(\frac{\omega\Delta t}{2}\right) - \frac{\sigma\sigma^*\left(\Delta t\right)^2}{4\varepsilon\mu}\cos^2\left(\frac{\omega\Delta t}{2}\right) - j\left(\frac{\sigma\Delta t}{4\varepsilon} + \frac{\sigma^*\Delta t}{4\mu}\right)\sin\left(\omega\Delta t\right) = S^2\left(W_x^2 + W_y^2 + W_z^2\right). \tag{42}$$

Here, the Courant factor is $S = c\,\Delta t/\Delta$, with c being the speed of light in the modeled media, $\Delta = \Delta x = \Delta y = \Delta z = \lambda_0/N_s$ the uniform spatial resolution, λ_0 the exact wavelength in the lossy material, N_s the spatial sampling rate, and Δt the time step size.

As done so far for RPIM, the analytical study was reproduced by using Yee's FDTD scheme; then the governing electromagnetic equations, the general Fourier mode insertion, and the linear homogeneous system are deduced. Finally, the dispersion relation in lossy media is obtained. We note that the FDTD dispersion relation in lossy media is similar to Equation (42), whereas the expressions of the W_ξ terms (for $\xi = x, y$ or z) should be $W_\xi = \sin(k_\xi \Delta\xi/2)$, even though the coefficients C_1, C_2, C_1', C_2', and S_ξ are identical for both dispersion relations.

Let us also consider the case in which equivalent magnetic losses σ^* are neglected. After some calculations, the dispersion equation is thus given by:

$$\sin^2\left(\frac{\omega\Delta t}{2}\right) - j\frac{\sigma\Delta t}{4\varepsilon}\sin(\omega\Delta t) = S^2\left(W_x^2 + W_y^2 + W_z^2\right). \tag{43}$$

These dispersion relations in lossy media are complex and lead to complex wavenumbers. However, if $\sigma = \sigma^* = 0$, Equation (42) is reduced to that for lossless media, for which the wavenumber becomes a purely real number. The resulting relation is reduced to:

$$\sin^2\left(\frac{\omega\Delta t}{2}\right) = S^2\left(W_x^2 + W_y^2 + W_z^2\right). \tag{44}$$

We should mention that the dispersion relation of the FDTD method in lossless media is also literally similar to Equation (44), with $W_\xi = \sin(k_\xi\Delta\xi/2)$ for $\xi = x, y$, or z. In the following section, a comparative study built on the numerical dispersion characteristics is performed for both methods.

5. NUMERICAL RESULTS

We now investigate and compare RPIM and FDTD dispersion characteristics in lossy media, such as numerical dispersion, loss error, and anisotropy. The following performance measures are defined herein, such as numerical phase error NPE and loss error NLE. In addition, to remove the angular dependence from NPE and NLE, the averaged corresponding quantities are defined. Hence, the average numerical phase error, loss error $ANPE$, and $ANLE$, respectively, for $M \times N$ preselected angles are given:

$$NPE = \frac{\beta - \beta_0}{\beta_0}, \quad ANPE = \frac{1}{M \times N}\sum_{n,m} NPE(\phi_n, \theta_m), \tag{45a}$$

$$NLE = \frac{\alpha - \alpha_0}{\alpha_0}, \quad ANLE = \frac{1}{M \times N}\sum_{n,m} NLE(\phi_n, \theta_m), \tag{45b}$$

where β and β_0 are the numerical and physical phase constants, and α and α_0 are the numerical and physical loss constants, respectively. Also $m = 1, 2, \ldots, M$ and $n = 1, 2, \ldots, N$, and $M = N = 91$ are chosen since it is the dispersion pattern period. Numerical anisotropy loss A_l and anisotropy dispersion A_d are defined as $A_l = (\alpha_{\max} - \alpha_{\min})/\alpha_{\min}$ and $A_d = (\beta_{\max} - \beta_{\min})/\beta_{\min}$, where $\alpha_{\max}$ and $\beta_{\max}$ are the maxima of the numerical loss and phase constants, respectively, when scanning in ϕ and θ, while $\alpha_{\min}$ and $\beta_{\min}$ are the corresponding minima. The Courant-Friedrichs-Lewy (CFL) number is defined as $S_{3D} = \Delta t/\Delta t_c$, where Δt_c is the CFL limit.

Similar to the range used in [9], the conductivity is selected to vary from 10^{-4} S/m to 30 S/m, thereby including the electric conductivity of most dielectric materials [15]. The operating frequency of the wave we are interested in is set to $f = 300$ MHz.

Figures 1 and 2 present NPE and NLE versus θ at $\phi = 45°$, where $0° \le \theta \le 90°$. The node sampling rate $N_s = 80$, CFL number $S_{3D} = 0.5$, and conductivity $\sigma = 15$ S/m. We note that the FDTD method exhibits low dispersion errors compared to RPIM but has larger NLE, except for $\theta = 0°$. The NPE and NLE for the two methods are equal.

As observed from Fig. 3, $ANPE$ increases with the conductivity σ for both methods, where FDTD has a lower $ANPE$. Fig. 4 shows that the RPIM exhibits a small $ANLE$ compared to FDTD within the range [11.07 S/m, 30 S/m] with $S_{3D} = 0.5$ and $N_s = 80$. However, for the range [0 S/m, 11.07 S/m],

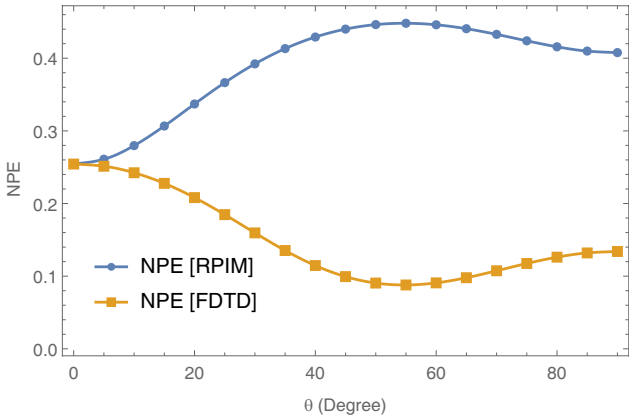

Figure 1. Numerical Phase Error for RPIM and FDTD with $\sigma = 15\,\mathrm{S/m}$, $N_s = 80$ and $S_{3D} = 0.5$ at $\phi = 45°$.

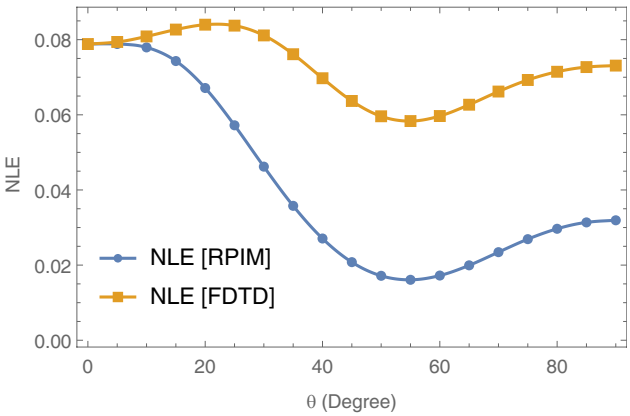

Figure 2. Numerical Loss Error for RPIM and FDTD with $\sigma = 15\,\mathrm{S/m}$, $N_s = 80$ and $S_{3D} = 0.5$ at $\phi = 45°$.

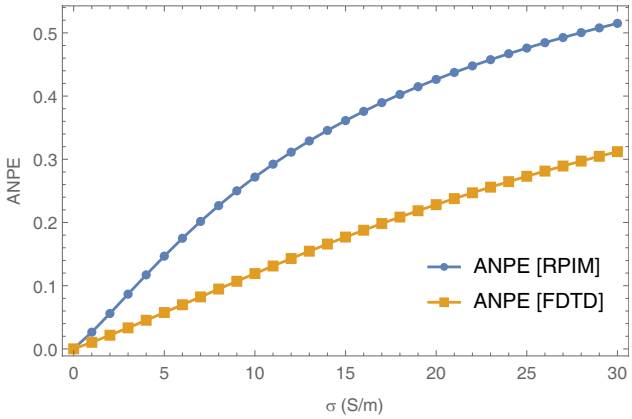

Figure 3. 3D Averaged Numerical Dispersion Error for RPIM and FDTD method with $S_{3D} = 0.5$.

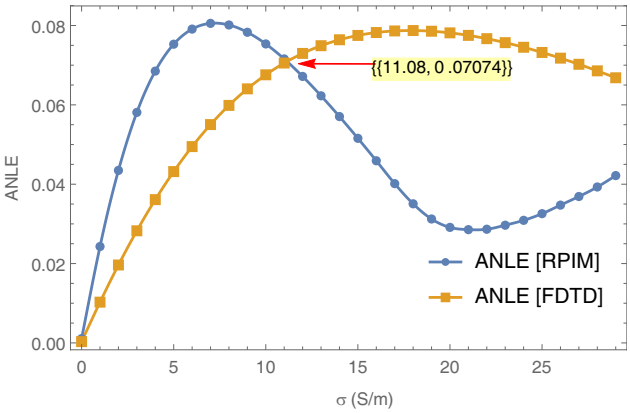

Figure 4. 3D Averaged Numerical Loss Error for RPIM and FDTD method with $S_{3D} = 0.5$.

this last behavior is inverted. On the other hand, for both methods the lossless case illustrates the expected absence of numerical losses.

Figures 5 and 6 illustrate that, although the FDTD method anisotropy dispersion is smaller than the RPIM one, the RPIM anisotropy loss is mainly lower than the FDTD method over a broad conductivity range delimited by 11 S/m and 30 S/m.

According to Fig. 5, the anisotropy dispersion increases with conductivity for both methods. However, Fig. 7 reveals that the anisotropy dispersion decreases when conductivity varies from zero to 0.0288 S/m and reaches its minimum at about 2.379×10^{-7} S/m. This behavior is hidden in Fig. 5 because the swept conductivity varies from 0 S/m to 30 S/m. The presence of these minima is exploited as an alternative to reduce numerical anisotropy dispersion, which affects the resonance frequency, by adding suitable electric losses when lossless media is considered.

6. NUMERICAL EXPERIMENTS

An accumulation of phase errors, resulting from numerical phase velocity errors, leads to a resonance variation over the frequency domain [16]. Thus, resonance frequency accuracy serves as a measure of anisotropy. This property will be exploited in this section.

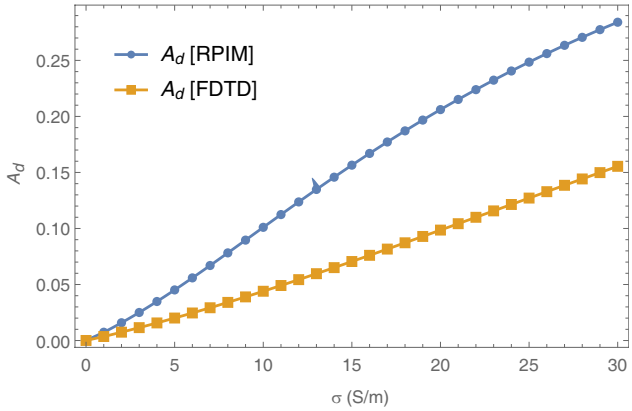

Figure 5. 3D Numerical Anisotropy Dispersion for RPIM and FDTD method with $S_{3D} = 0.5$.

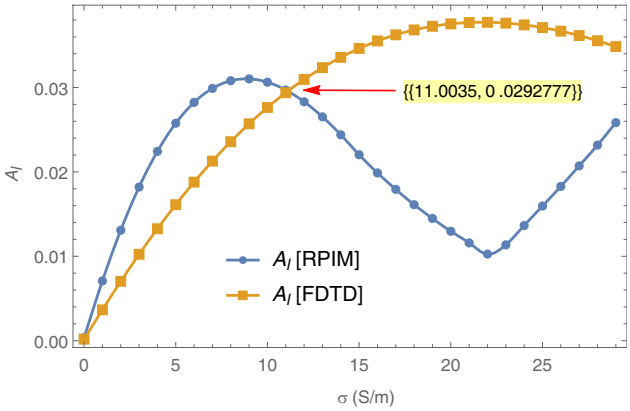

Figure 6. 3D Numerical Anisotropy Loss for RPIM and FDTD method with $S_{3D} = 0.5$.

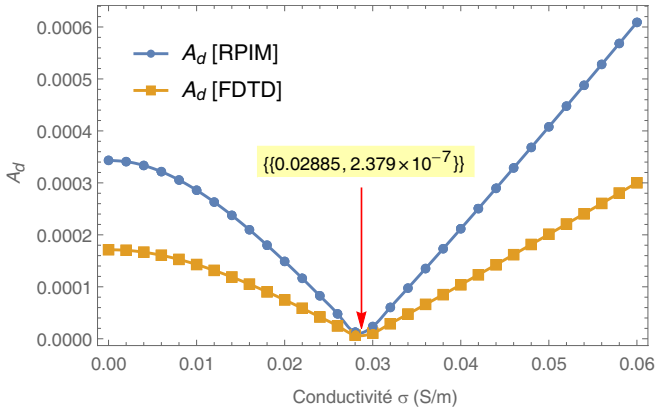

Figure 7. 3D Numerical Anisotropy Dispersion for RPIM and FDTD with $S_{3D} = 0.5$, and $N_s = 80$.

As illustrated in Fig. 7, numerical anisotropy dispersion decreases over the range of [0 S/m, 0.0288 S/m] until it reaches a minimum at $\sigma = 0.0288$ S/m, for the operating frequency. Accordingly, loss addition in lossless media decreases A_d and thereby improves resonance frequency accuracy for $\sigma < 0.0288$ S/m.

6.1. 2D Square Cavity

In order to validate the numerical results above, we consider a 2D square cavity $\lambda \times \lambda$, filled with a homogeneous lossy media and terminated by PEC walls. The origin is at the lower-left corner of the domain. In conjunction with the Cartesian directions, the sampling rate of spatial nodes is fixed at $\Delta x = \Delta y = \lambda/20$. In similar fashion to [11] and [13], the domain is uniformly discretized using double staggered E/H grids. The electromagnetic fields are fed by a TM line source and estimated by RPIM under the assumption that TM_{21} cavity mode is excited. The excitation is a modulated Gaussian pulse given by: $J_z(A, n) = \exp[-((n\Delta t - 4\sigma)/(\sqrt{2}\sigma))^2] \sin[2\pi f(n\Delta t - 4\sigma)]$. The width factor is $\sigma = 1.061$ ns; the CFL number $S_{2D} = 0.5$; and the observation point is at $B(72\,\text{cm}; 52\,\text{cm})$. A set of RPIM parameters, transcendentally introduced, is selected so that the shape parameter $\alpha = 18$, the maximum distance $r_{\max} = 7.3$ cm, and the number of nodes in the support domain $N = 12$.

Figure 8 shows a comparison between lossless and lossy ($\sigma = 0.0002$ S/m) cases for time-domain E_z field component variations computed with the RPIM at observation point B. The introduced losses decrease the electric field amplitude owing to a slight increase in physical losses, which in turn produce

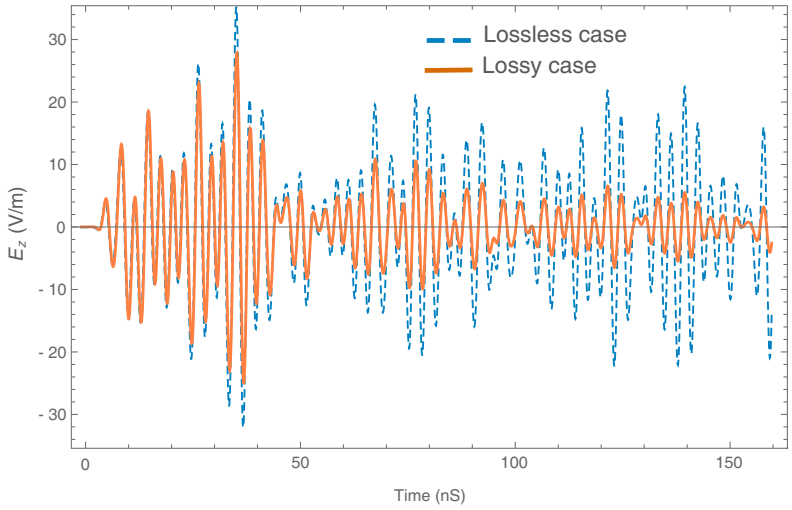

Figure 8. Time domain of E_z component at the observation point for a duration of 160 ns.

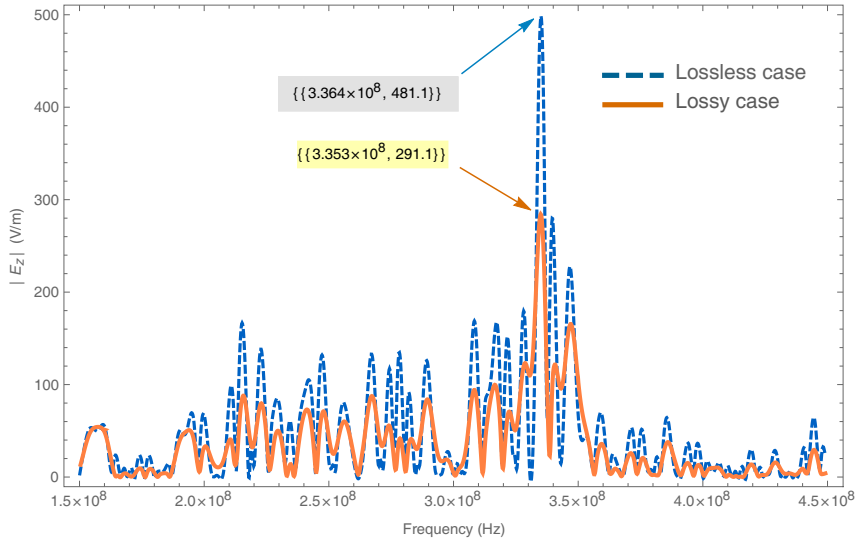

Figure 9. Normalized frequency domain of E_z component at the observation point with $S_{3D} = 0.5$.

numerical losses. Fig. 9 shows the electric field modulus versus frequency, which validates that the cavity resonant frequency reaches essentially the value found in the reference case with a relative error estimated to 1/10 of lossless case, evaluated to 0.29%.

6.2. Double-Ridge Cavity

Fig. 10 shows the geometry of the double-ridge cavity with perfect conducting walls and with dimensions $\lambda \times \lambda \times 0.3\lambda$ at $f = 3\,\text{GHz}$. The excitation is a modulated Gaussian pulse placed at point $A(0.015\,\text{m};\ 0.05\,\text{m};\ 0.0175\,\text{m})$ and the observation point at $B(0.085\,\text{m};\ 0.05\,\text{m};\ 0.0175\,\text{m})$. The width factor is $\sigma = 0.940\,\text{ns}$ and the CFL number $S_{3D} = 0.5$. The number of nodes in the support domain is $N = 8$ as shown in Fig. 11; the shape parameter $\alpha = 0.7$; and the sampling rate of spatial nodes is fixed at $\Delta x = \Delta y = \Delta z = \lambda/20$. From Fig. 12, the relative error is estimated to 1.75% for lossless case and 0.07% for the lossy case. For the first resonant frequency of the double-ridge rectangular cavity, we took an average over those mentioned [17, 18]; thus, we have used the reference frequency $f_{\text{ref}} = 2.787\,\text{GHz}$.

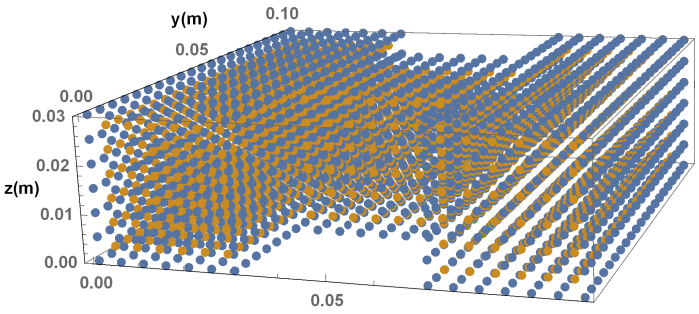

Figure 10. Node distributions of the H-cavity.

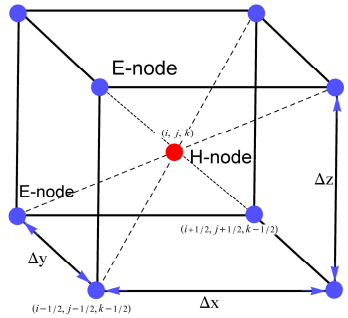

Figure 11. H-node support domain.

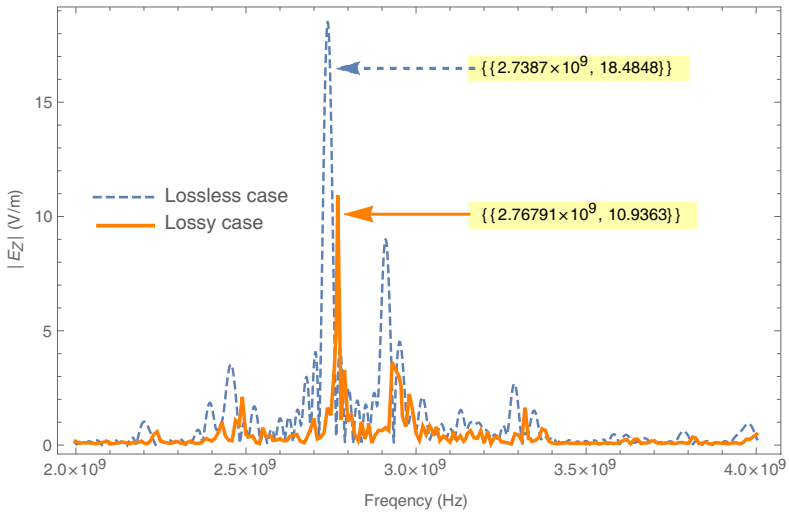

Figure 12. E_z component at the observation point of the double ridged cavity.

7. CONCLUSION

In this paper, 3D-RPIM governing electromagnetic equations are formulated in matrix form. The numerical dispersion characteristics, based on the general Fourier mode, are also investigated. In addition, the 3D-RPIM and 3D-FDTD dispersion relations in lossy media are deduced. The analytical difference between those dispersion relations is the expression of the W_ξ term, for $\xi = x, y$, or z. Newton's method is used to solve the dispersions relations for the RPIM and FDTD methods. Numerical results showed that FDTD is less dispersive than RPIM. In contrast, RPIM presents lower numerical losses in a wide conductivity range varying from 11 S/m to 30 S/m with $N_s = 80$. Moreover, for $\sigma = 0.0288$ S/m, both methods produce numerical anisotropy dispersion of 2.379×10^{-7}, which can be considered null. The RPIM algorithm is implemented in such a way to minimize A_d and improve the frequency resonance accuracy. For a square cavity, the accuracy of the resonance frequency varies from 0.29% ($\sigma = 0$ S/m) to 0.029% ($\sigma = 2 \times 10^{-4}$ S/m), and for the double ridged cavity, it varies from 1.75% to 0.07%, which is in reasonable agreement with the theoretically predicted results.

REFERENCES

1. Sadasiva, M. R., *Time Domain Electromagnetics,* Academic Press, 1999.
2. Liu, G. R., *Mesh-Free Methods Moving beyond the Finite Element Method,* CRC Press, 2003.

3. Kaufmann, T., Y. Yiqiang, C. Engström, Z. Chen, and C. Fumeaux, "Recent developments of the meshless radial point interpolation method for time-domain electromagnetics," *International Journal of Numerical Modelling: Electronic Networks, Devices and Fields*, Vol. 25, 468–489, 2012.
4. Angulo, A., L. P. Pozo, and F. Perazzo, "A posteriori error estimator and an adaptive technique in meshless finite points method," *Eng. Anal. Bound. Elem.*, Vol. 33, No. 11, 1322–1338, 2009.
5. Kaufmann, T., C. Engström, and C. Fumeaux, "Residual-based adaptive refinement for meshless eigenvalue solvers," *2010 International Conference on Electromagnetics in Advanced Applications*, 244–247, Sydney, Australia, 2010.
6. Liu, G. R. and Y. T. Gu, *An Introduction to Meshfree Methods and Their Programming,* Springer, 2005.
7. Taflove, A. and S. C. Hagness, *Computational Electrodynamics: The Finite Difference Time-Domain Method,* Artech House, 2000.
8. Yang, S., Z. Chen, Y. Yu, and S. Ponomarenko, "On the numerical dispersion of the radial point interpolation meshless method," *IEEE Micr. and Wir. Comp. Let.*, Vol. 24, No. 10, 653–655, October 2014.
9. Fu, W. and E. L. Tan, "Stability and dispersion analysis for ADI-FDTD method in lossy media," *IEEE Trans. on Ant. and Prop.*, Vol. 55, No. 4, 1095–1102, April 2007.
10. Zhang, X., Y. Peng, Z. D. Chen, and Y. Yu, "Numerical dispersion analysis of radial point interpolation meshless method," *2017 Progress in Electromagnetics Research Symposium — Fall (PIERS — FALL)*, 717–719, Singapore, November 19–22, November 2017.
11. Lee, J.-F., R. Lee, and A. Cangellaris, "Time-domain finite-element methods," *IEEE Trans. on Ant. and Prop.*, Vol. 45, No. 3, 430–442, March 1997.
12. José, A. P., G. Ana, G. Oscar, and V. Angel, "Analysis of two alternative ADI-FDTD formulations for transverse-electric waves in lossy materials," *IEEE Trans. on Ant. and Prop.*, Vol. 57, No. 7, 2047–2054, July 2009.
13. Hichem, N. and A. Taoufik, "Unconditional stability analysis of the 3D-radial point interpolation method and Crank-Nicolson scheme," *Progress In Electromagnetics Research M*, Vol. 68, 119–131, 2018.
14. Strikwerda, J. C., *Finite Difference Schemes and Partial Differential Equations*, Wadawoth Brooks/Cole Advanced Books Software, Pacific Grove, CA, 1989.
15. Pozar, D. M., *Microwave Engineering,* 3rd Edition, Wiley, New York, Wiley, 2005.
16. Zhang, Y., S. W. Lü, and J. Zhang, "Reduction of numerical dispersion of 3-D higher order alternating-direction-implicit finite-difference time-domain method with artificial anisotropy," *IEEE Trans. on Ant. and Prop.*, Vol. 57, No. 7, 2416–2428, 2009.
17. Chen, T. S., "Calculation of the parameters of the ridged waveguides," *IRE Transactions on Microwave Theory and Techniques*, 12–17, January 1957.
18. Balanis, C. A., *Advanced Engineering Electromagnetics,* 2nd Edition, John Wiley and Sons, 2012.
19. Yu, Y. and Z. Chen, "A 3-D radial point interpolation method for meshless time-domain modeling," *IEEE Transactions on Microwave Theory and Techniques*, Vol. 57, No. 8, 2015–2020, August 2009.
20. Chen, Z., C. -F. Wang, and W. J. R. Hoefer, "A unified view of computational electromagnetics," *IEEE Transactions on Microwave Theory and Techniques*, Vol. 70, No. 2, 955–969, February 2022.
21. Juntunen, J. S. and T. D. Tsiboukis, "Reduction of numerical dispersion in FDTD method through artificial anisotropy," *IEEE Transactions on Microwave Theory and Techniques*, Vol. 48, No. 4, 582–588, April 2000.